MNRAS **000**, 1–12 (0000) Preprint 2 August 2016 Compiled using MNRAS LATEX style file v3.0

The Volumetric Rate of Superluminous Supernovae at $z \sim 1$

S. Prajs[1]⋆, M. Sullivan[1], M. Smith[1], A. Levan[2], N. V. Karpenka[1], T. D. P. Edwards[3], C. R. Walker[4], W. M. Wolf[5], C. Balland[6], R. Carlberg[7], D. A. Howell[8,9], C. Lidman[10], R. Pain[6], K. Perrett[11], C. Pritchet[12], V. Ruhlmann-Kleider[13]

[1]*Department of Physics and Astronomy, University of Southampton, Southampton, SO17 1BJ, UK*
[2]*Department of Physics, University of Warwick, Coventry, CV4 7AL, UK*
[3]*GRAPPA Institute, University of Amsterdam, Science Park 904, 1090 GL Amsterdam, Netherlands*
[4]*Jodrell Bank Centre for Astrophysics, School of Physics and Astronomy, The University of Manchester, Manchester M13 9PL, UK*
[5]*Kavli Institute for Theoretical Physics, University of California, Santa Barbara, CA 93106, USA*
[6]*Astrophysics Research Institute, Liverpool John Moores University, IC2, Liverpool Science Park, 146 Brownlow Hill, Liverpool L3 5RF, UK*
[6]*LPNHE, CNRS-IN2P3 and University of Paris VI & VII, F-75005 Paris, France*
[7]*Department of Astronomy and Astrophysics, University of Toronto, 50 St. George Street, Toronto, ON M5S 3H8, Canada*
[8]*Las Cumbres Observatory Global Telescope, 6740 Cortona Dr., Suite 102, Goleta, CA 93111, USA*
[9]*Department of Physics, University of California, Santa Barbara, CA 93106, USA*
[10]*Australian Astronomical Observatory, North Ryde, NSW 2113, Australia*
[11]*Defence Research and Development Canada, 3701 Carling Avenue, Ottawa, Ontario K1A 0Z4*
[12]*Department of Physics and Astronomy, University of Victoria, P.O. Box 3055, Victoria, BC V8W 3P6, Canada*
[13]*CEA, Centre de Saclay, Irfu SPP, 91191 Gif-sur-Yvette, France*

2 August 2016

ABSTRACT

We present a measurement of the volumetric rate of superluminous supernovae (SLSNe) at z∼1.0, measured using archival data from the first four years of the Canada-France-Hawaii Telescope Supernova Legacy Survey (SNLS). We develop a method for the photometric classification of SLSNe to construct our sample. Our sample includes two previously spectroscopically-identified objects, and a further new candidate selected using our classification technique. We use the point-source recovery efficiencies from Perrett et al. (2010) and a Monte Carlo approach to calculate the rate based on our SLSN sample. We find that the three identified SLSNe from SNLS give a rate of 91^{+76}_{-36} SNe Yr^{-1} Gpc^{-3} at a volume-weighted redshift of $z = 1.13$. This is equivalent to $2.2^{+1.8}_{-0.9} \times 10^{-4}$ of the volumetric core collapse supernova rate at the same redshift. When combined with other rate measurements from the literature, we show that the rate of SLSNe increases with redshift in a manner consistent with that of the cosmic star formation history. We also estimate the rate of ultra-long gamma ray bursts (ULGRBs) based on the events discovered by the *Swift* satellite, and show that it is comparable to the rate of SLSNe, providing further evidence of a possible connection between these two classes of events. We also examine the host galaxies of the SLSNe discovered in SNLS, and find them to be consistent with the stellar-mass distribution of other published samples of SLSNe.

Key words: supernovae: general – surveys

1 INTRODUCTION

Superluminous supernovae (SLSNe), defined as events with an absolute magnitude brighter than −21 ($M < -21$), are a new puzzle in the study of supernovae (Gal-Yam 2012). They appear 50-100 times brighter than normal supernova events, and form at least two distinct classes: SLSNe-II, which show signatures of interaction with circumstellar material (CSM) via hydrogen and other lines (Ofek et al. 2007; Smith et al. 2007; Drake et al. 2011), and SLSNe-I (or SLSNe-Ic), which are hydrogen poor (Quimby et al. 2011). While SLSNe-II may naturally be explained as an extension of the fainter type IIn supernova events, the power source behind SLSNe-I remains a subject of debate.

The most popular model in the literature to explain SLSNe-I involves energy input from the spin-down of a newly-formed magnetar following a core-collapse supernova (Kasen & Bildsten 2010; Woosley 2010; Inserra et al. 2013), although alternative models involving pulsational pair instability supernovae (Woosley et al. 2007; Yan et al. 2015) or interaction with a hydrogen-free CSM

⋆ E-mail: S.Prajs@soton.ac.uk

(Chevalier & Irwin 2011; Chatzopoulos et al. 2013; Sorokina et al. 2015) have also been proposed. Additional clues are also provided by the environments in which SLSNe-I occur: predominantly vigorously star-forming and low-metallicity dwarf galaxies (e.g., Lunnan et al. 2014; Leloudas et al. 2015; Chen et al. 2016). This preference for low-metallicity environments is supported by the modelling of the SLSN-I spectra, which favours a fairly low metal abundance (Mazzali et al. 2016).

Of particular note is the rarity of SLSN-I events. It took many years for the first events to be identified as such (Quimby et al. 2007; Barbary et al. 2009), and for the class to be recognised (Quimby et al. 2011), in part due to their blue and relatively featureless optical spectra. Even after several years of study, only around 25 well-observed SLSNe-I exist (e.g., see compilations in Inserra & Smartt 2014; Papadopoulos et al. 2015; Nicholl et al. 2015a). Initial estimates placed the rate of SLSNe-Ic at less than one for every 1000 core collapse supernovae (Quimby et al. 2011), and more recent studies are broadly consistent with this (Quimby et al. 2013; McCrum et al. 2015). However, there has been no direct measurement of the SLSN-I rate for a well-controlled optical transient survey. Such a measurement can provide constraints on progenitor models, as there must, at the very least, be a sufficient number of any putative progenitor system to produce the observed SLSN rate. Furthermore, if the strong preference for a young, low-metallicity environment reflects a real physical effect, any evolution in the SLSN rate with redshift should also track the cosmic star-formation and metal enrichment history of the Universe, and the underlying evolving populations of galaxies.

In this paper, we present such a measurement of the volumetric rate of SLSNe using data taken from the Supernova Legacy Survey (SNLS), part of the Canada-France-Hawaii Telescope Legacy Survey (CFHT-LS). SNLS observed four square degrees of sky for six months per year over the course of five years, with a primary goal of locating and studying type Ia supernovae (SNe Ia) to measure the equation-of-state of dark energy (Astier et al. 2006; Sullivan et al. 2011). A by-product of this search was a deep, homogeneous catalogue of optical transients down to a limiting magnitude of $i \sim 24$ (Perrett et al. 2010), with more than 500 optical transient spectra, including two confirmed SLSNe-I (Howell et al. 2013). This, combined with a significant amount of ancillary redshift information in the search fields (e.g., Ilbert et al. 2006; Lilly et al. 2007; Le Fèvre et al. 2013; Lidman et al. 2013), makes it a perfect controlled dataset for the study of supernova rates (Neill et al. 2006; Bazin et al. 2009; Perrett et al. 2012), including SLSNe.

This paper is presented as follows. In Section 2 we describe our model for selecting SLSNe, in terms of a magnetar model that can reproduce the optical luminosity evolution of these events. Section 3 introduces the SNLS dataset, and discusses the methods for identifying and selecting SLSNe from its archive. Section 4 focuses on the Monte Carlo method used to compute the rate of SLSNe using detection efficiencies measured from the SNLS data. The results are compared against other SLSN rate measurements in Section 5, and we summarize in Section 6. Throughout, we assume a Hubble constant of $H_0 = 70\,\mathrm{km\,s^{-1}\,Mpc^{-1}}$ and a flat ΛCDM universe with $\Omega_M = 0.3$, and all magnitudes are given in the AB photometric system.

2 SELECTING SUPERLUMINOUS SUPERNOVAE

Our first task is to develop a method for the photometric selection of optical transients that will enter our SLSN sample. Although SLSNe are often defined as supernovae with an absolute magnitude in the u-band, M_u, of $M_u < -21$ (Gal-Yam 2012), we do not use this definition for two reasons. The first is that there are now several examples in the literature of events that are spectroscopically similar to SLSNe-I, but that do not pass this formal threshold. Examples of these include events such as DES13S2cmm (Papadopoulos et al. 2015) and PTF11rks (Inserra et al. 2013). The second reasons is the recent discovery of new classes of fast and luminous transients (Arcavi et al. 2016) with luminosities similar to SLSNe, but with a faster light curve evolution and different spectroscopic types. Therefore, in place of an arbitrary magnitude cut, we use a photometric classification approach built around a simple analytical model that provides a good fit to a sample of confirmed SLSNe-I. This approach implies that our rate is calculated only for objects which are similar to the sample of confirmed SLSNe-I. This may not capture all objects of this class at the currect time due to small size of the training sample.

There are two main ingredients that we need for our SLSN modelling: an underlying model for the time-dependent bolometric luminosity of a SLSN-I, and a spectral energy distribution (SED) that can convert this bolometric luminosity into time-evolving spectra. From this spectral series, synthetic photometry in any desired filter and at any desired redshift can be calculated for comparison to observed data. We discuss each of these ingredients in turn.

2.1 Magnetar model

Early studies used a simple expanding photosphere radiating as a cooling black body to represent the SLSN-I light curves (eg. Howell et al. 2013). This approach provides a good approximation around the peak of the light curve, but it begins to significantly deviate from the data at 30 days after maximum light (Fig. 1). Instead we use the currently popular magnetar model, which is able to reproduce the photometric behaviour for the entire SLSN-I population (Inserra et al. 2013; Nicholl et al. 2013), in particular at late times.

In the magnetar model, the bolometric luminosity, L, as a function of time t for a homologously expanding ejecta is (Arnett 1982)

$$L(t) = 4.9\times10^{46}\, e^{-(t/\tau_\mathrm{m})^2}\,\delta(t)\int_0^t \frac{2t'}{\tau_\mathrm{m}^2}\, e^{(t'/\tau_\mathrm{m})^2}\,\frac{B_{14}^2\,P_\mathrm{ms}^{-4}}{\left(1+t'/\tau_\mathrm{p}\right)^2}dt', \qquad (1)$$

where τ_m is the diffusion timescale, B_{14} is the neutron star magnetic field in units of 10^{14} G, P_ms is the magnetar spin period in ms, $\delta(t)$ is the deposition function or trapping coefficient, and τ_p is the magnetar spin-down timescale, inferred from B_{14} and P_ms (see Appendix D of Inserra et al. 2013, and references therein for full details).

The trapping coefficient, $\delta(t)$, is often assumed to be unity (i.e., implying the full trapping of the high-energy photons radiated by the magnetar within the supernova ejecta) and time-independent (Inserra et al. 2013; Papadopoulos et al. 2015; Nicholl et al. 2015a). Here we use a correction introduced by Wang et al. (2015) with a time-dependent trapping coefficient of

$$\delta(t) = 1 - \exp\left(-\frac{9\kappa \mathrm{M}_\mathrm{ej}^2}{40\pi E_k}t^{-2}\right), \qquad (2)$$

where $\mathrm{M_{ej}}$ is the ejecta mass, E_k is the explosion energy, and κ is the opacity. $\mathrm{M_{ej}}$ is proportional to τ_m, E_k and κ (Inserra et al. 2013). We fix the explosion energy to be $E_k = 10^{51}$ erg and the opacity as $\kappa = 0.1\,\mathrm{cm^2 g^{-1}}$ following other studies (e.g. Inserra et al. 2013; Inserra & Smartt 2014; Nicholl et al. 2015a; Papadopoulos et al.

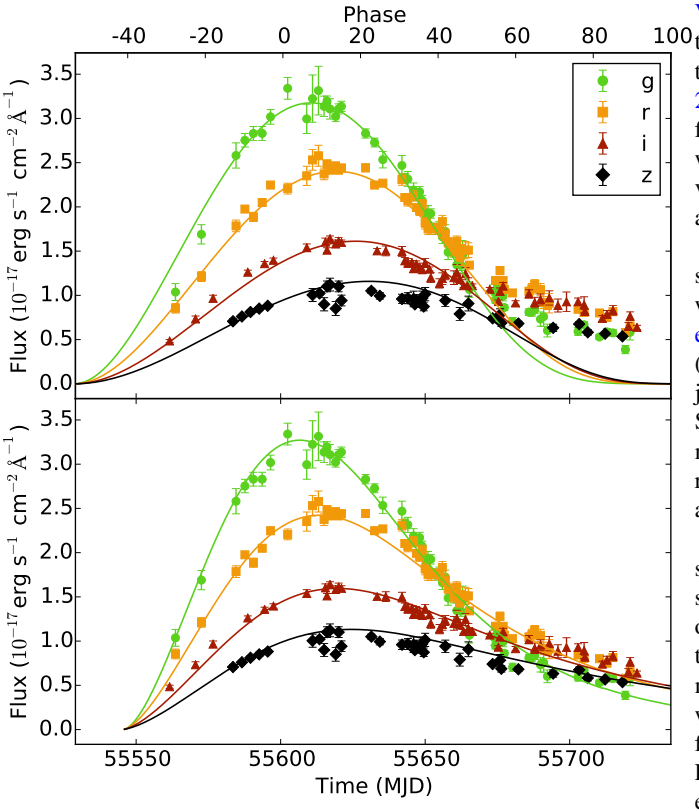

Figure 1. The SLSN-I PS1-11ap *griz* light curve (McCrum et al. 2014) compared to two models describing its photometric evolution. In the upper panel, the model is a simple expanding and cooling black body fitted to data around maximum light only, and in the lower panel the model is our 'absorbed' magnetar model fitted to the entire light curve. In the case of the magnetar model, the spectrum of SNLS-06D4eu (Howell et al. 2013) has been used as an absorption template in the modelling of the SED (see Section 2.2). Note that while both models can produce reasonable fits around the peak of the light cuve, the black body model is not able to reproduce the characteristic late-time behaviour of SLSNe. Light curve phases are measured with respect to peak brightness in the rest-frame *u*-band as predicted by our magnetar model fit.

2015). Using this time-dependent trapping coefficient improves the late-time fit to the light curve. For a typical SLSN we calculate $\delta \simeq 1$ up to 75 days post explosion. However, as the ejecta opacity to high energy photons decreases with time we find $\delta \simeq 0.8$ at 150 days post explosion, emphasising the importance of this correction in the late time light curves.

We use the equations derived in Appendix D of Inserra et al. (2013) to relate the magnetar model parameters described above to the photospheric radius and temperature and their time evolution. The photospheric radius is proportional to the ejecta velocity, which is also a function of the kinetic energy and M_{ej}. Thus, using Planck's law the magnetar model parameters can also be used to generate a simple smooth SED. In the next section, we discuss how we adjust this SED to physically resemble the spectra of SLSNe-I.

2.2 Spectral energy distributions

The spectra of SLSNe-I are relatively featureless in the rest-frame optical, with characteristic broad lines of O II, and evolve slowly (Chomiuk et al. 2011; Howell et al. 2013; Papadopoulos et al. 2015; Vreeswijk et al. 2014). However, there are much stronger absorption features in the rest-frame ultraviolet (UV), with features attributed to Mg II, Fe III, C II, Co III, Si III and Ti III (see Mazzali et al. 2016, for line identifications). This UV SED is of prime importance for our study, as it is redshifted into the optical at high redshift where our search is most sensitive and where we probe the largest volume. Thus it is important to construct our magnetar model with an appropriate SED for our *k*-corrections to be realistic.

The number of SLSNe-I with good UV coverage remains small. We construct SED templates from three example SLSN which have a good coverage in the UV: iPTF13ajg (Vreeswijk et al. 2014), SCP06F6 (Barbary et al. 2009) and SNLS-06D4eu (Howell et al. 2013). In each case we use one spectrum per object, as spectral time series are only available for iPTF13ajg and SCP06F6; for these objects we use the spectrum closest to maximum light. Our spectral templates cover a rest-frame wavelength range of 1620–3320 Å (SNLS-06D4eu), 1800–3800 Å (SCP06F6) and 1800–5250 Å (iPTF13ajg).

We follow Vreeswijk et al. (2014), fitting Planck's law to several featureless, 50 Å wide, continuum regions in the observed spectra of our three events with a good UV coverage (Fig. 2), in order to estimate the black body continuum. We then use the ratio between the observed spectra and these blackbody continua as measure of the strength of the absorption features as a function of wavelength in the different spectra. The result is a multiplicative function that, when combined with a black body continuum from Planck's law, can reproduce an observed SLSN-I spectrum on any epoch (Fig. 2). We assume that the red part of the optical SED not covered by our templates follows a black body, and for the blue part we linearly extrapolate the SEDs to lower wavelengths from the bluest 200Å of the template (Fig. 2). This combination of the magnetar model and our UV SED templates results in a significant improvement in the light curve fits compared to the simpler expanding and cooling black body model (Fig. 1).

2.3 Superluminous supernova definition

Our final step is to select parameters of the magnetar model that define the extent of SLSN-I parameter space using a training sample of suitable events. Only a small number of published spectroscopically confirmed SLSNe-I have data of sufficient quality to constrain their luminosity, rise and decline time, as well as the colour evolution. We therefore introduce data-quality cuts in the published sample: we select only objects observed with a minimum of two epochs in at least three filters before maximum light, and two epochs in at least three filters between maximum light and +30 days, where maximum light is measured in the rest-frame *u*-band. 15 events which pass these cuts and form our training sample are listed in Table 1. We have corrected all the published photometry for Milky Way extinction, and set an arbitrary error floor of 0.03 magnitudes for all photometric points to account for possible systematic uncertainties that were not included in the published data.

We fit the training sample light curves with the magnetar model. We calculate the bolometric luminosity from eqn. (1) and eqn. (2), and estimate the photospheric radius using equations from Inserra et al. (2013). The Stefan-Boltzmann law then gives the photometric temperature. From these, we calculate the black body SED from Planck's law, apply the absorption template, place at the correct redshift, and integrate through the observed filters on the epochs data were obtained. We use all three spectral absorption templates for each event, and retain only the best fitting template (see Table 2).

Table 1. The training sample of SLSNe-I.

SN Name	Redshift	Survey	Reference
PTF12dam	0.108	Palomar Transient Factory	Nicholl et al. (2013)
SN2011ke	0.143	Catalina Real-Time Transient Survey & Palomar Transient Factory	Inserra et al. (2013)
SN2010gx	0.230	Palomar Transient Factory	Pastorello et al. (2010)
SN2013dg	0.265	Catalina Real-Time Transient Survey	Nicholl et al. (2014)
PS1-11ap	0.524	Pan-STARRS	McCrum et al. (2014)
DES14X3taz	0.608	Dark Energy Survey	Smith et al. (2016)
PS1-10bzj	0.650	Pan-STARRS	Lunnan et al. (2013)
DES13S2cmm	0.663	Dark Energy Survey	Papadopoulos et al. (2015)
iPTF13ajg	0.741	intermediate Palomar Transient Factory	Vreeswijk et al. (2014)
SNLS-07D2bv	1.500	SNLS	Howell et al. (2013)
SNLS-06D4eu	1.588	SNLS	Howell et al. (2013)

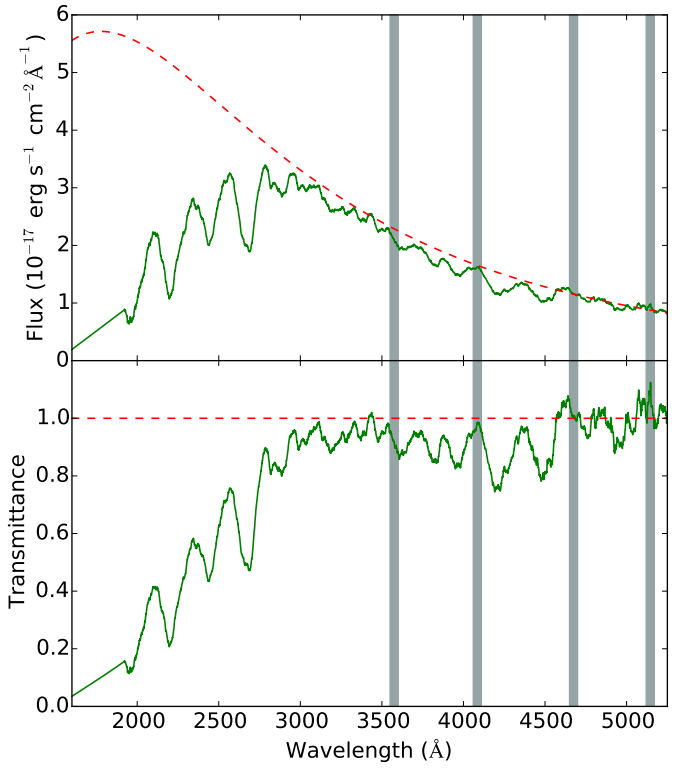

Figure 2. Contructing template SEDs for SLSNe-I. Upper panel: the spectrum of iPTF13ajg (solid; Vreeswijk et al. 2014) fitted to Planck's law (dashed) in narrow, 50 Å, continuum regions (vertical bands). There is a good agreement between the black body and the data in the region $\lambda > 3000$ Å, with stronger absorption features appearing further blueward. Lower panel: the ratio between the observed spectrum and the continuum fit giving the absorption strength as a function of wavelength. This can then be used to improve the accuracy of the UV SED by combining it with a time dependent black body (Section 2.2).

The parameter estimation is performed using MultiNest (Feroz & Hobson 2008; Feroz et al. 2009, 2013), an implementation of the nested sampling algorithm that is particularly suited to complex probability distributions, run in multi-modal mode. Our fit parameters are τ_m, B_{14}, P_{ms}, and the explosion date, t_{expl}. We also fit for host-galaxy extinction, parametrised using the colour excess $E(B-V)_{host}$, using the small magellanic cloud (SMC) extinction law (Gordon et al. 2003) with $R_V = 2.7$. This extinction law is measured in environments that most likely resemble the metal poor and star-forming dwarf galaxies associated with the hosts of SLSNe-I. We use a uniform prior on all fit parameters with the boundary values (Table 3) chosen arbitrarily to allow a large margin between the prior edge and the fit parameters for the training sample of SLSNe-I. For host galaxy extinction, we allow $E(B-V)_{host}$ to vary between 0 and 0.2 mag, typical for extinctions measured directly from spectroscopy of SLSN-I host galaxies (Leloudas et al. 2015), and typical of extinctions present in low stellar-mass galaxies (Garn & Best 2010).

The magnetar model provides a good fit to all the SLSNe-I that we selected for our sample. Table 2 contains the fit parameters, as well as two additional derived parameters: the peak absolute magnitude in the Sloan Digital Sky Survey u-band filter (M_u; York et al. 2000), and the rise-time, t_{rise}, measured from explosion to maximum light in the rest-frame u-band. Note that the M_u are given in the AB magnitude system; $M_u^{AB} \simeq M_u^{vega} + 0.9$ (Blanton & Roweis 2007). Thus while some of the training sample have $M_u^{AB} > -21$, none have $M_u^{vega} > -21$.

Fig. 3 shows the best fit magnetar model parameter space. We define the SLSN-I parameter space using an ellipsoid that is the lowest volume, simple geometric body consistent will all the SLSN-I training sample. We use the Khachiyan algorithm (Aspvall & Stone 1980; Khachiyan 1980) to find the smallest volume enclosing all points (see Appendix A for the parametrisation). Fig. 3 shows the three two-dimensional projections of this parameter space, populated with our training sample of literature SLSNe-I.

The SLSN-I parameter space can now be used to classify further objects that are not in our training sample by fitting the magnetar model to those data and examining where their resulting best fits lie compared to the parameter space defined by the training sample. Ideally, we would now test this by fitting a second sample of known SLSN-I events. However, the number of events is so small that it is not currently possible to construct such a sample, and have enough objects to construct the parameter space in Fig.3. Thus we assume that the parameter space in Fig. 3 is defined by a representative sample of events. We also note that the fitting method and SLSN-I definition makes no assumption about the luminosity of the event; it is quite possible for fit events to have $M_u > -21$ and still be classified as SLSNe.

While the magnetar model is used to describe the physical processes behind SLSNe-I, it is possible that, due to the flexibility of

Table 2. Magnetar model parameters for the sample of 15 published SLSNe.

Name	M_u	$t_{\rm rise}$ (days)	$\tau_{\rm m}$ (days)	B_{14} ($\times 10^{14}$ G)	$P_{\rm ms}$ (ms)	$t_{\rm expl}$ (MJD)	$E(B-V)$	χ^2_ν	Template
PTF12dam	-21.4	34.72	22.15	0.78	2.85	56044.5	0.18	2.49	06D4eu
SN2011ke	-21.2	24.84	30.61	3.67	2.13	55647.5	0.01	1.31	iPTF13ajg
SN2010gx	-21.7	24.56	30.36	3.20	1.54	55247.1	0.19	0.86	06D4eu
SN2013dg	-21.2	25.37	28.05	3.30	2.75	56412.3	0.07	0.23	SCP06F6
PS1-11ap	-21.8	32.1	20.08	0.79	2.51	55559.0	0.02	1.62	06D4eu
DES14X3taz	-21.7	47.21	26.16	0.23	1.67	57019.2	0.09	5.18	06D4eu
PS1-10bzj	-21.2	22.17	18.44	2.65	3.84	55524.0	0.07	0.37	06D4eu
DES13S2cmm	-20.0	30.7	21.19	1.28	5.29	56509.0	0.01	0.51	06D4eu
iPTF13ajg	-22.4	31.45	33.41	1.57	1.32	56346.9	0.19	0.30	iPTF13ajg
07D2bv	-21.1	28.41	36.88	3.40	2.18	54132.4	0.05	0.41	SCP06F6
06D4eu	-21.9	21.48	29.94	3.82	1.00	53956.3	0.11	1.26	06D4eu

Table 3. Priors on the fit parameters in the magnetar model

Parameter	Lower limit	Upper limit
$\tau_{\rm m}$ (days)	10	100
B_{14} (10^{14} G)	0.1	20
$P_{\rm ms}$ (ms)	1	20
$E(B-V)_{\rm host}$	0.001	0.2

the model, it could also produce a good fit to SLSNe-II even though the underlying physical model in SLSNe-II is believed to be different. We are unable to test this robustly as there are currently only two known SLSNe-II with sufficient coverage to pass our quality cuts (Inserra et al. 2016). We therefore refer to events that lie in our parameter space as 'SLSN-I-like' events. We thus calculate the rate of objects which are well-represented by this model and are similar to the published SLSNe. This does not exclude the possibility that there may be further objects of this class that we are unable to identify in our sample.

3 THE SUPERNOVA LEGACY SURVEY DATASET

We next describe the observational dataset on which we will make the volumetric rate measurement. We first introduce the survey itself, and then discuss our selection of candidate SLSNe from the archive of variable objects.

3.1 The Supernova Legacy Survey

The SLSN-I dataset for our volumetric rate calculation is taken from the Supernova Legacy Survey (SNLS; Astier et al. 2006; Guy et al. 2010). SNLS was a rolling transient survey using the MegaCam detector (Boulade et al. 2003) at the 3.6-m Canada-France-Hawaii Telescope, operating from 2003-2008. The survey imaged four, one-square degree deep fields (D1 to D4; field centres can be found in Sullivan et al. 2006) in four SDSS-like filters (g_M,r_M,i_M,z_M) every 3–5 days during dark and grey time, over six months in each year. The photometric search was accompanied by a dedicated spectroscopic follow-up survey that classified ~500 supernovae (Howell et al. 2005; Ellis et al. 2008; Balland et al. 2009; Walker et al. 2011). Although the search continued throughout 2008, the original i_M-band filter was damaged in July 2007 (see Betoule et al. 2013) and data from beyond this date are not included in this analysis. This leaves just over four years of imaging used here.

The SNLS detected 4949 transient objects using a difference-imaging pipeline (Perrett et al. 2010), including many objects visually designated as active galactic nuclei (AGN) and variable stars, as well as supernovae. The pipeline used to detect the transients and perform photometry was designed to operate in real-time on fast timescales, usually <24 hours, to allow for a rapid spectroscopic prioritisation (Sullivan et al. 2006) and follow-up (Perrett et al. 2010). We have since performed more accurate 'offline' photometry for all the SNLS candidates using a well-established supernova photometry pipeline (see Firth et al. 2015, and references therein). In addition, for our best candidates, we have measured multi-season light curves to check for long-term activity typical of AGN.

3.2 Identifying SLSNe in SNLS

SNLS spectroscopically confirmed two SLSNe-I: SNLS-07D2bv at $z = 1.500$ and SNLS-06D4eu at $z = 1.588$ (Howell et al. 2013). Both objects were initially classified from real-time photometry (Sullivan et al. 2006) as low probability SN Ia candidates, and targeted for low priority spectroscopic follow-up. These objects form part of our training sample of published SLSNe-I (Section 2.3).

Two further SLSN-I candidates have since been detected in deep, stacked SNLS images (Cooke et al. 2012), with host galaxy redshifts of $z = 2.04$ and $z = 3.89$. These objects were not, however, discovered in the real-time SNLS pipeline as they were fainter than the single-epoch detection limits, and thus do not form part of the sample in this paper.

We search in the SNLS transient database for additional SLSN candidates that are well fit by our model from Section 2. We assign redshift information as follows. 1694 have spectroscopic redshifts, either from spectra of the transients (Balland et al. 2009; Bronder et al. 2008; Ellis et al. 2008; Howell et al. 2005) or of the host galaxy from redshift catalogues in the SNLS search fields (e.g., Lilly et al. 2007; Le Fèvre et al. 2013; Lidman et al. 2013). Where a spectroscopic redshift is not available, we use photometric redshift estimates from Ilbert et al. (2006), which provides photometric redshift information for galaxies in the SNLS fields at $i_M < 25$ with a median uncertinty of $\delta z = 0.1$. SNLS transients are associated to potential host galaxies by selecting the nearest galaxy within a radius of 1.5″. This provides photometric redshift information on a

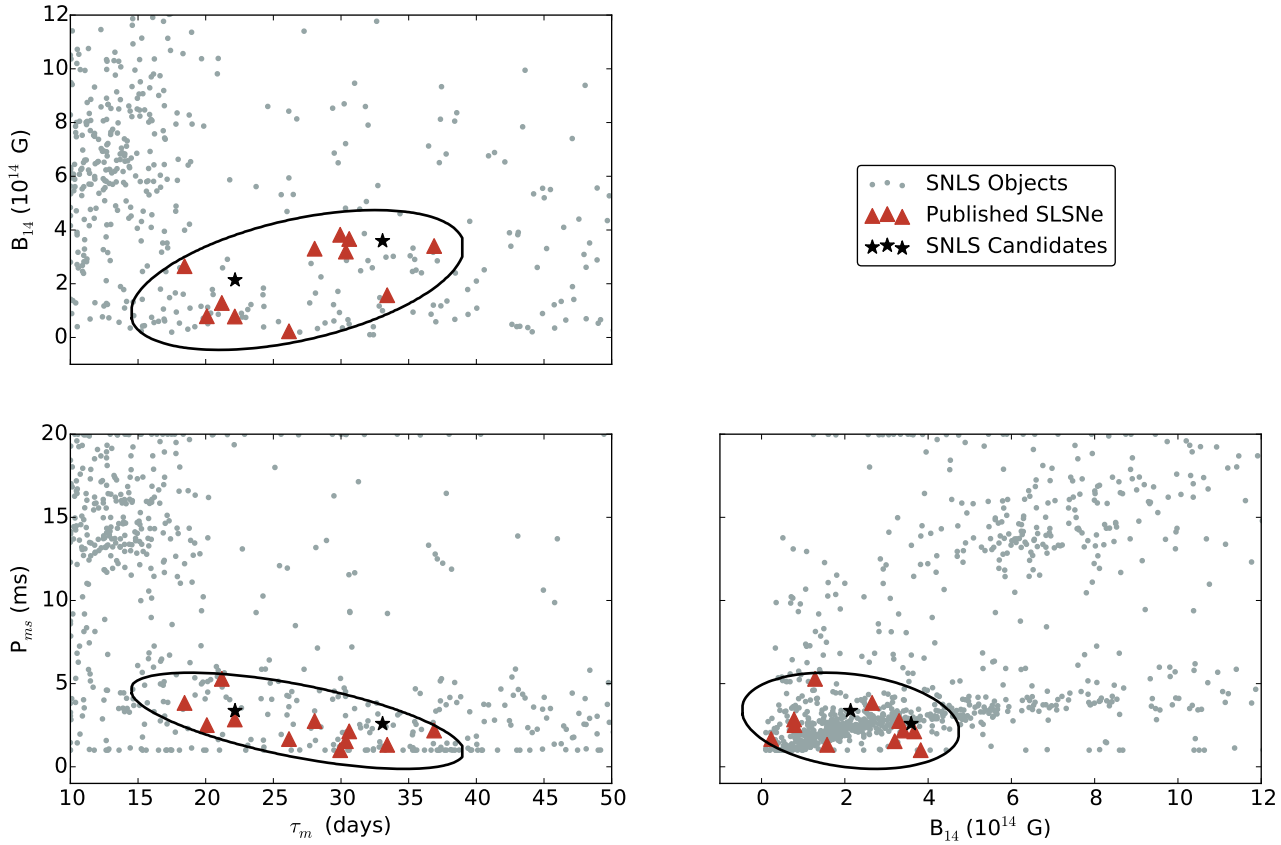

Figure 3. The $\tau_{\rm m}$–B_{14}–$P_{\rm ms}$ parameter space constructed from the magnetar model fits as described in Section 2.1. The SNLS objects are denoted by grey circles. The ellipses correspond to the two dimensional projections of the three dimensional ellipsoid, fitted around the parameter space of the known SLSNe-I (shown as triangles) to form a region defining them in terms of the model. The SNLS candidates that fall within this parameter space are shown as stars.

further 1527 events. For these transients, we use a range of redshift values in the fits spanning the photometric redshift uncertainties.

We are then left with 1728 candidates with no redshift information. Inspecting the light curves showed that only 292 of these were likely to be real objects with multiple detections in multiple bands. The remainder are likely false detections that incidentally matched the SNLS real-time detection criteria (Perrett et al. 2010). For these last objects, we assign a broad range of redshifts ($0.2 \leq z \leq 1.6$ in steps of $\Delta z = 0.1$) and treat then identically to objects with a known redshift. While we might naively expect the number of hostless supernovae to be higher, the depth of the SNLS deep stacks is good enough to measure photometric redshifts for all but the very faintest host galaxies.

We fit all the SNLS objects using the three available absorption templates, retaining the parameters corresponding to the best fit only. During the fitting, we apply the same quality cuts as for our training sample: two detections in at least three filters between the fit explosion date and maximum light, and a further two detections in at least three filters between maximum light and +30 days. Here, we consider a detection to be $\geq 5\,\sigma$ in the real-time photometry. Of the 4949 SNLS transients, 2097 pass these data quality cuts, and the position of their best-fitting magnetar model parameters can be see in Fig. 3.

As would be expected, our magnetar model is not a good fit to the majority of the SNLS objects. We remove the bulk of these poor fits using a conservative cut at a χ^2 per degree of freedom (χ^2_ν) of 20. Such a large χ^2_ν cut is designed to retain all SLSNe (see Table 2 for typical χ^2_ν for SLSNe), even those where a part of the light curve may not be well-represented by our model, such as the pre-peak 'bump' observed in some SLSNe (Nicholl et al. 2015b; Nicholl & Smartt 2015; Smith et al. 2016).

Of the SNLS objects that pass our data quality and χ^2_ν cuts, four lie within the parameter space of SLSNe-I as defined in Section 2. This includes the two spectroscopically confirmed events from Howell et al. (2013) that were part of our training sample. For the other two candidates, SNLS-05D3ks and SNLS-07D3bs, we measure the multi-season light curves (see Section 3.1) and visually inspect them to search for signatures of any long-term variability or detections prior to, or sufficiently after, the putative supernova event. This process of visual inspection eliminats SNLS-05D3ks which shows clear multiple maxima spanning three years (Fig. 4), leaving just a single, new SLSN-I-like candidate: SNLS-07D3bs.

3.3 SNLS-07D3bs

SNLS-07D3bs was identified as a SLSN candidate between $0.6 < z < 1.2$ based on its host galaxy photometric redshift estimate, with a best fit to the magnetar model at z=1.0 (see Fig. 5) using the spectrum of SNLS-06D4eu as the UV template. SNLS-07D3bs was observed spectroscopically during SNLS on 2007 April 17 at the Keck-I 10-m telescope using the Low Resolution Imaging Spectrograph (LRIS), but no spectral classification could be made from the data at the time (Fakhouri 2013).

However, at that time the SLSN-I class was not known and

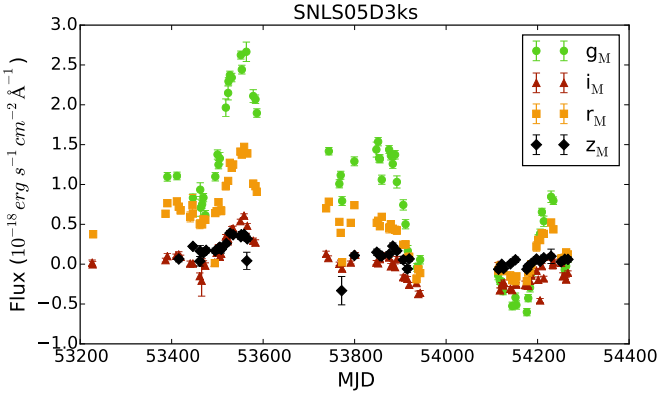

Figure 4. The g_M, r_M, i_M, z_M multi-season light curve of SNLS-05D3ks. This transient was found within the SLSN-I parameter space (Fig. 3), but did not pass visual inspection as it shows clear signs of multiple maxima.

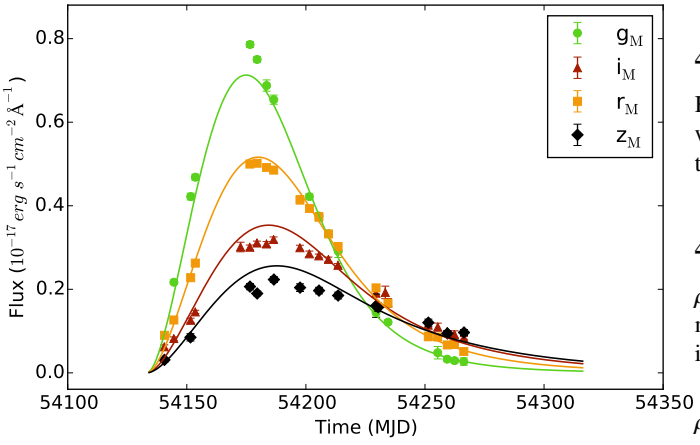

Figure 5. The g_M, r_M, i_M, z_M light curve of SNLS-07D3bs overplotted with the best fit magnetar model (Section 2) at $z = 0.757$. The candidate shows a good agreement with the model.

no SLSN-I spectral templates were available for comparison with the data. Therefore, using the SUPERFIT spectrum identification tool (Howell et al. 2005), we have re-analysed the spectrum of SNLS-07D3bs. The data are noisy (signal-to-noise ~ 7) as observing conditions were quite poor, but we find the best spectral match to be to the SLSN-I iPTF13ajg at $z = 0.757$ (Fig. 6). While this is clearly an uncertain spectral classification, there is no evidence from the spectrum that the object is not a SLSN, and the best match is an event of that type. The magnetar model also provides a good fit at that redshift (see Table 4 for the magnetar model fit parameters). The host galaxy (RA=14^{h}21^{m}50^s.466, Dec.=+53^{d}10^{m}28^s.58) galaxy was detected in the SNLS deep stack images (Ilbert et al. 2006), but is very faint, with AB magnitudes of (u_M, g_M, r_M, i_M, z_M) = (26.61±0.49, 26.13±0.16, 25.67±0.13, 25.18±0.11, 25.19±0.37). Taking the evidence together, we consider SNLS-07D3bs to be the third SLSN detected by the real-time pipeline of SNLS.

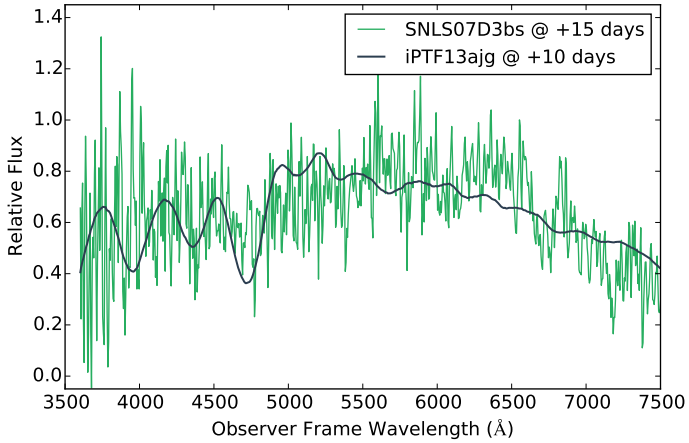

Figure 6. The spectrum of SNLS-07D3bs from Keck-I/LRIS, taken 15 rest-frame days after maximum light. The signal-to-noise of the spectrum is low preventing a definitive classification; however, the spectrum is consistent with a SLSN at around $z = 0.76$. Weak galaxy emission lines are consistent with $z = 0.757$.

4 THE RATE OF SUPERLUMINOUS SUPERNOVAE

Having identified a sample of three SLSNe in SNLS, in this section we now calculate the volumetric rate of SLSNe ($\rho_{\rm slsn}$) implied by these detections.

4.1 Method

$\rho_{\rm slsn}$ is defined as a sum over the N SLSNe found in a given co-moving search volume V over a search duration T, weighted by the inverse of the detection efficiency, ϵ_i, of detecting each event, i.e.,

$$\rho_{\rm slsn} = \frac{1}{V}\sum_{i}^{N}\frac{(1+z_i)}{\epsilon_i T_i}. \quad (3)$$

The factor $(1+z_i)$ corrects for time dilation. The detection efficiency ϵ_i is a statistic describing how each SLSN should be weighted relative to the whole population; $1-\epsilon_i$ gives the fraction of similar SLSNe that exploded during the search period but were missed by the survey due to (for example) search inefficiencies.

Our SLSN-I detection efficiencies are based on the analysis of Perrett et al. (2010), who carried out a study of the detection efficiencies and selection biases of type Ia supernovae (SNe Ia) in SNLS, and subsequently calculated a rate of those events in Perrett et al. (2012). In this study, several million fake SNe Ia were placed in the SNLS science images, with the correct temporal evolution, and passed though the SNLS real-time detection pipeline. The recovery efficiencies of these SNe Ia could then be estimated. Although these results were produced using a particular model of a particular supernova type, at a more basic level they also provide the recovery efficiencies of point sources in the SNLS data as a function of magnitude in *every* i_M-band image that SNLS took, and it is these more basic data that we use in this study.

We reverse the common approach to supernova rate calculations: instead of calculating the rate of SLSNe starting with the number of detected objects, we instead calculate the probability that a given input value of $\rho_{\rm slsn}$ will lead to an eventual detection of three SLSNe in the SNLS survey. This method also produces a non-Gaussian uncertainty estimate as a by-product of the calcula-

Table 4. Magnetar model parameters for the new SNLS SLSN candidate: SNLS-07D3bs.

Name	M_u	$t_{\rm rise}$ (days)	$\tau_{\rm m}$ (days)	B_{14} ($\times 10^{14}$ G)	$P_{\rm ms}$ (ms)	$t_{\rm expl}$ (MJD)	$E(B-V)$	χ^2_ν	Template
SNLS-07D3bs	-20.9	27.2	23.7	2.28	3.81	54132.5	0.05	1.96	iPTF13ajg

tion in the form of a rate probability distribution (Fig. 7). We quote the uncertainties as the 1-σ confidence region of this distribution.

We simulate the SLSN population using a Monte Carlo approach, exploding SLSNe randomly within the SNLS search period and search volume, and creating artificial SLSN light curves on each epoch on which SNLS took data, including the effect of $1+z$ time dilation. This gives an i_M apparent magnitude on each epoch, which can be compared to the point-source recovery statistics on that epoch to give the probability of detection.

4.2 Search volumes

The effective SNLS search areas in each field from which the search volumes can be calculated can be found in (Perrett et al. 2012); the total search area is 3.56 deg^2. The volume is calculated by considering the redshift range to which our search is sensitive. There is a small variation in the detection efficiency amongst the fields; D3 observing season was longer in comparison to the other fields while D1 and D2 had on average, marginally deeper exposures.

At the low-redshift end, the search volume is set by the redshift at which a SLSN would become saturated in the SNLS data. At the high-redshift end, the volume is set by the redshift at which we are no longer able to recover a SLSN event, i.e. a SLSN would fall below the detection limit of the survey.

Fig 8 illustrates the redshift range to which we are sensitive, showing the recovery efficiency as a function of redshift for the three SNLS events from Section 3.2. For events at $z < 0.2$, the efficiency drops rapidly due to saturation effects, and thus we choose $z = 0.2$ as the lower redshift limit. At the upper redshift limit, we choose $z = 1.6$; although events similar to SNLS-06D4eu are detectable to beyond $z = 2$, the fainter events like SNLS-07D3ds will become undetectable in some of the SNLS search fields beyond $z = 1.6$.

4.3 Rate calculation

We begin each Monte Carlo simulation with an input $\rho_{\rm slsn}$ value. From this we calculate the number of SLSNe that would have occurred within the SNLS search area over the redshift range to which we are sensitive ($0.2 < z < 1.6$) in bins of $\Delta z = 0.01$. We assume that this rate does not evolve within the redshift range which we consider in our simulation (we test this assumption below). The artificial SLSNe are then assigned a random spatial position (and consequent Milky Way extinction), redshift, host galaxy extinction and physical parameters drawn from the magnetar model parameter space derived from our training sample (Fig. 3). A random explosion epoch during the SNLS search period is assigned to each event, and the predicted photometry calculated on every epoch corresponding to a SNLS observation.

Using the point-source detection efficiencies of Perrett et al. (2010), we can then calculate the probability of detecting each SLSN on every epoch of i_M data, and combine the probabilities to give the total probability of discovering each object. In order to be considered detected, we also enforce that each artificial SLSN must pass the same data quality cuts as both our training sample (Section 2.3) and our real sample of SNLS candidates (Section 3.2). We repeat the entire simulation 100,000 times over an input $\rho_{\rm slsn}$ range of $5 \leq \rho_{\rm slsn} \leq 500$ SNe Yr^{-1} Gpc^{-3}.

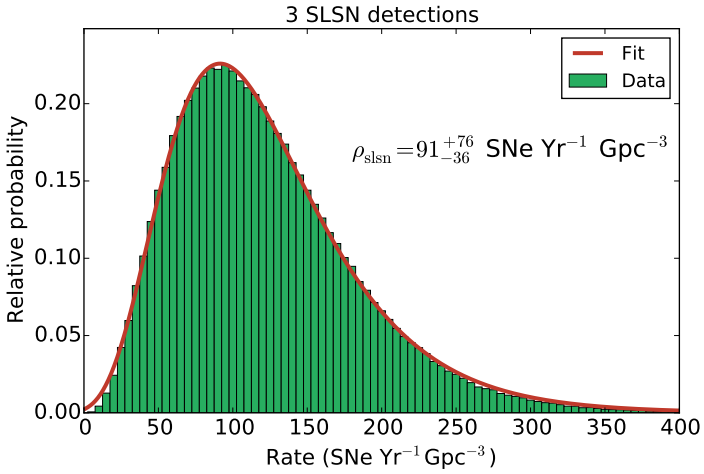

Figure 7. The probability distribution of the volumetric rate of SLSNe for the three SLSN candidates over the duration of SNLS at $0.2 < z < 1.6$, as determined by our 100,000 Monte Carlo simulations. A log-normal distribution is fitted to the data (red line) to estimate the peak of the probability distribution and the uncertainties, quoted as the 68% confidence region.

Fig. 7 shows the probability of three SLSN events being detected in our simulations as a function of this input rate. A log-normal distribution was fitted to the simulation results and used to smoothly determine the peak of the distribution as well as the 1σ confidence regions. From this, we find the rate of SLSNe at $z = 1.13$ (the volume-weighted centre of the $0.2 < z < 1.6$ range) to be $\rho_{\rm slsn} = 91^{+76}_{-36}$ SNe Yr^{-1} Gpc^{-3}.

We also investigate the effect that our assumption of a uniform redshift distribution in the simulated SLSNe may have on our final rate. We repeat the Monte Carlo simulation, but instead draw the SLSNe from a redshift distribution that follows the cosmic star-formation history (SFH; taken from Hopkins & Beacom 2006). We find $\rho_{\rm slsn} = 98^{+82}_{-39}$ SNe Yr^{-1} Gpc^{-3}, close to our original result and, considering the uncertainities, a negligible difference. Thus our final rate, averaged over the redshift range we have considered, is not sensitive to the assumed rate evolution in our simulation. This is likely due to the relative uniformity of our detection efficiency as a function of redshift within our search volume (see Fig. 8).

5 DISCUSSION

In Fig. 9, we compare our new SLSN rate measurement with other published values taken from the literature (Quimby et al. 2013;

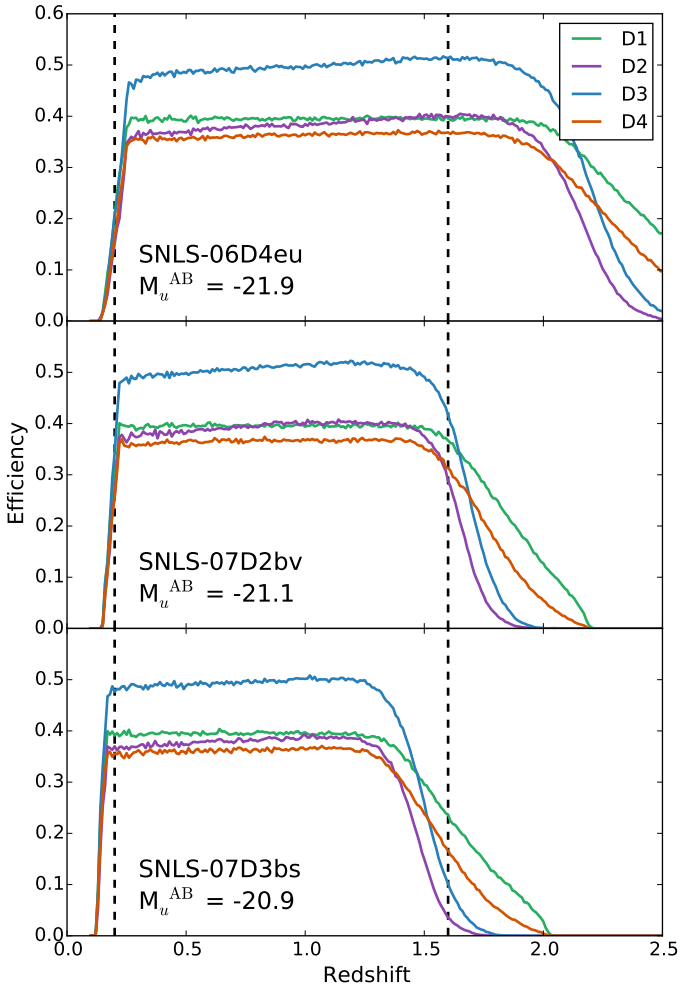

Figure 8. The redshift range to which our SLSN search is sensitive, as a function of the four SNLS search fields. The figure shows the recovery efficiency of three different SLSNe as a function of redshift, with each line corresponding to a different search field.. The efficiency includes the same data quality cuts as used in the training sample in Section 2.3 and the SNLS candidate selection in Section 3.2. The vertical dashed lines at $z = 0.2$ and $z = 1.6$ illustrate the final redshift range used in our Monte Carlo rate calculations.

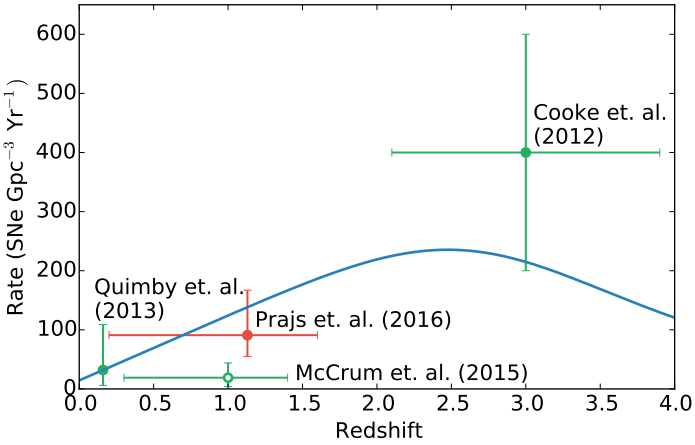

Figure 9. The evolution of the volumetric SLSN rate as a function of redshift. We show measurements by Quimby et al. (2013), McCrum et al. (2015) and Cooke et al. (2012) for comparison. The McCrum et al. (2015) result is marked by an open circle to highlight that it may not be directly comparable with the other measurements as it is derived by a comparison to the rate of core collapse supernovae and is not a direct measurement. The observed evolution is consistent with that of the SFH over the same redshift range; we over-plot in blue the parametrisation of the cosmic SFH of Hopkins & Beacom (2006), normalised to the low-redshift SLSN-I rate obtained by Quimby et al. (2013).

Cooke et al. 2012) as a function of redshift. We observe an increase in the volumetric rate as a function of redshift. The extent of this observed evolution is consistent with the evolution in the cosmic star-formation history (SFH) observed over the same redshift range (Hopkins & Beacom 2006). This is, perhaps, an unsurprising result, as SLSNe are thought to originate from the death of very massive and hence short-lived stars (Nicholl et al. 2015a,b). However, we note that we cannot discriminate between the evolution that follows the SFH, and one with the same evolution to $z = 1.5$ followed by a peak at a much higher redshift, as the $z > 1.5$ measurement is quite uncertain.

A higher-redshift peak may be expected due to the association of SLSNe with metal-poor galaxies. SLSNe-I almost invariably explode in galaxies that are low-mass, compact dwarfs (Neill et al. 2011; Lunnan et al. 2015), and that are metal-poor and strongly star-forming (Lunnan et al. 2013; Chen et al. 2013; Leloudas et al. 2015). One popular interpretation of this is that the low metallicity must play a role in the formation of SLSNe-I, which is consistent with the low metal content inferred from their UV spectra (Mazzali et al. 2016). This scenario would also predict a volumetric rate evolution that follows both the cosmic SFH and cosmic chemical enrichment. Further $z > 2$ rate measurements are needed to test this in more detail.

Fig. 10 shows the distribution of SLSN host-galaxy stellar masses as measured by Lunnan et al. (2014). We use the ZPEG photometric redshift package (Le Borgne & Rocca-Volmerange 2002) with the SNLS multi-waveband g_M,r_M,i_M,z_M host galaxy photometry to estimate the stellar mass for SNLS-07D3bs. We are not able to derive host galaxy stellar masses for SNLS-06D4eu and SNLS-07D2bv using the SNLS deep stacks due to the galaxies faintness and the lack of infrared (rest-frame optical) data. We instead use values obtained by Leloudas et al. (2015) and Schulze et al. (in prep.). The host stellar masses for all three of our candidates agree with the published SLSN-I host stellar mass distribution (Fig. 10).

Using SLSNe discovered by the Pan-STARRS medium deep survey over $0.3 \leq z \leq 1.4$, McCrum et al. (2015) measure the relative rate of SLSNe to be between $3^{+3}_{-2} \times 10^{-5}$ and $8^{+2}_{-1} \times 10^{-5}$ that of the core-collapse supernova rate (ρ_{cc}). We use the SNLS ρ_{cc} measurement at $z \sim 0.3$ of $1.42 \pm 0.6 \times 10^{-4}$ SNe Gpc^{-3} yr^{-1} (Bazin et al. 2009), and extrapolate it to $z = 1.13$, assuming it tracks the cosmic SFH, increasing the rate by a factor of 2.62. Our own absolute SLSN rate can then be expressed as rate relative to that of core collapse SNe, which we find to be $2.2^{+1.8}_{-0.9} \times 10^{-4}$ of the ρ_{cc}. This is higher than, but still consistent with, the relative rate of McCrum et al. (2015).

5.1 Comparison with the rate of ULGRBs

There have been recent suggestions (Greiner et al. 2015) that ultra-long gamma ray bursts (ULGRBs; e.g., Gendre et al. 2013; Levan et al. 2014), with prompt gamma-ray emission lasting 10^3 to 10^4 s,

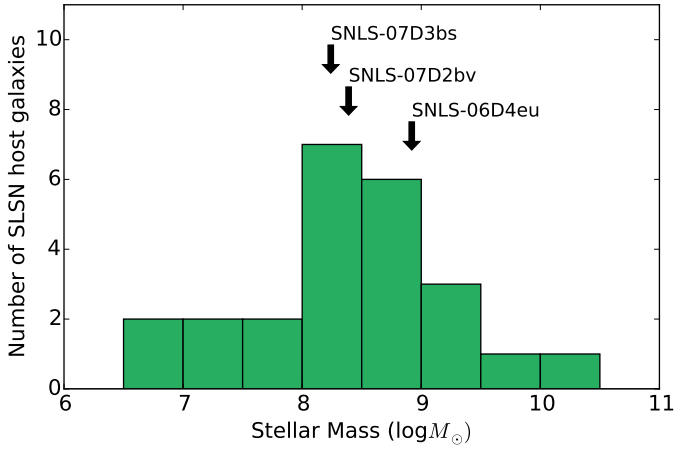

Figure 10. The stellar mass distribution of SLSN host galaxies plotted using the data from Lunnan et al. (2014), showing the consistency of SNLS07D3bs with the rest of the population. The lack of detections for the hosts of the high redshift candidates is consistent with being associated with low mass galaxies, found below the detection limit of SNLS at their redshifts.

could also be powered by the spin-down of a magnetar, in a similar mechanism to that suggested for SLSNe, albeit with different initial conditions explaining the physical differences between the phenomena (Mazzali et al. 2014). If both classes of objects were to originate in a similar physical scenario, one might expect their progenitors (and hence their rates) to be related.

The rate of ULGRBs is challenging to constrain. Bursts can be detected by the *Swift* satellite Burst Alert Telescope (BAT), but can have different triggering criteria: objects can be detected based on the detector rate over some given time period, or a search of the image plane, or their total fluence. A burst that misses one trigger, may still satisfy a different one at later times. This is particularly true for very long events, where a burst may go undetected by the rate triggers, or even by searches of the image plane on short time scales (e.g., 64 s). However they may then be recovered in image searches on longer time-scales of > 1000 s, as is the case for several very long events such as GRB 101225A (Thöne et al. 2011) and *Swift* J1644+57 (Levan et al. 2011; Burrows et al. 2011).

However, it is still possible to crudely estimate upper and lower limits to the rate of ULGRBs. The observed rate of a given individual burst is given by (Coward et al. 2012; Gendre et al. 2013)

$$\rho_{\rm ulgrb} = \frac{1}{V_{\rm max} T \Omega \eta_z} f_b, \quad (4)$$

where $V_{\rm max}$ is the maximum volume over which a burst could be detected, T is the time period over which the search was detected (10 years for *Swift*), the factor of Ω corrects for the fraction of the sky observed by *Swift* at a given time ($\Omega = 0.17$; Gehrels et al. 2004) and η_z reflects that many bursts do not have a known redshift, and so the realistic rate is higher by a corresponding factor (we assume $\eta_z = 0.3$; e.g. Jakobsson et al. 2006, 2012; Howell et al. 2014). Finally, f_b is the beaming factor of the burst, reflecting the number of bursts that are viewed off-axis to us and are hence undetected; $f_b = 2/\theta_j^2$, where θ_j is the opening angle of the GRB jet.

Determination of $V_{\rm max}$ and f_b can be difficult. In particular, $V_{\rm max}$ depends on the evolution of the burst properties (light curve and spectrum) with redshift, and how this is then convolved with the instrument triggering thresholds. However, we estimate this by assuming that the signal-to-noise of the detection scales with the square of the distance, and hence calculate the redshift at which a burst would pass the detection threshold (7σ). f_b can be determined for a given burst by the so-called 'jet-break', at which the later expansion of the jet creates an achromatic steepening of the observed afterglow emission (Levan et al. 2014).

We determine a pessimistic and realistic rate of ULGRBs. For our pessimistic rate we include only the few well-studied ULGRBs (GRB 101225A, 111209A, 121027, 130925A) and omit the very long events suggested to be tidal disruption flares. The maximum redshifts at which these events could be detected are $z = 0.9, 1.3, 2.3, 0.6$ respectively, with the mean $V/V_{\rm max} = 0.5$. As the mean redshift of this sample is similar to that of our SLSN-I sample, we can directly compared these measurements. The rate of ULGRBs is then $\rho_{\rm ulgrb} = 7 \times 10^{-2} f_b$ Gpc^{-3} yr^{-1}.

This is however a lower limit, as it is clear from observations of *Swift* bursts that other events have similar properties, but may not have been studied in depth at late times. The analysis of Zhang et al. (2014) suggests that ~ 15 bursts have engines active for > 5000 s. Our estimated rate should therefore be increased by a factor of four, assuming that these bursts belong to the same class of events as ULGRBs. This is however only a lower limit in the correction as their analysis was unable to firmly locate the end of the engine activity for < 50 per cent of these events.

Additional objects could be added in the very longest outbursts, typically assumed to be relativistic tidal flares (Bloom et al. 2011; Cenko et al. 2012; Brown et al. 2015), but with some similarities to SLSNe (Levan et al. 2016). The longest bursts are difficult to detect because of the trigger thresholds. Indeed, the very longest image triggers can only be used in cases where the dwell of *Swift* (i.e., how long it spends in a given observation) is longer than the length of the image trigger. This is only true for 15 per cent of the mission (Levan et al. 2014), causing a further factor of six increase in the rate that may be applicable for the longest events. In practice this would increase the sample size modestly (by a factor of two in extreme case). It should also be noted that the very long events by no means uniquely trigger these very long triggers. Therefore we estimate the realistic rate of ULGRBs to be $\rho_{\rm ulgrb} \approx 0.1 - 0.6 f_b$ Gpc^{-3} yr^{-1}, with the upper limit comparable to, although slightly lower than, the rate of long GRBs.

The final correction arises from the beaming rate. To date, jet-breaks have not been observed in ULGRBs, and the limits on the beaming angles (for typical ISM parameters) are around 12 degrees, indicating a beaming correction factor of order 50. The upper range of the ULGRB rate would then be $\rho_{\rm ulgrb} \approx 5 - 30$ Gpc^{-3} yr^{-1}. This is interestingly close to the SLSN-I rate we have measured at a similar redshift. If the physical mechanism responsible for driving the SN in GRB 111209A is the same as that responsible for other ULGRBs, and for creating the luminosity in SLSNe-I, then one should expect that a ULGRB would be observed for some observer in a significant fraction (and potentially all) of the SLSNe-I. This means that late-time observations could reveal off-axis afterglow-like emission at radio or X-ray wavelength in SLSNe-I. While one plausible example has been found in the bright late-time (100+ day) X-ray emission of SCP06F6 (Levan et al. 2013), other observations may suggest that such a ratio is unlikely. In any case, further multi-wavelength, late-time observations of SLSNe are clearly motivated.

6 SUMMARY

In this paper, we have used data from the SNLS to calculate the volumetric rate of SLSNe at $z \sim 1.1$. We used a simple magnetar model, in conjunction with new spectral templates, to develop a method for photometric classification of SLSNe. After fitting the magnetar model to a set of 11 well-sampled SLSN events from the literature, we have identified a region of parameter space that defines that literature sample.

We applied this criteria to the SNLS archival data and discovered (or recovered) three SLSN-I candidates within the redshift range of our rate calculation, two of which have previously been identified. We performed a Monte Carlo simulation of the SNLS to determine the rate of SLSNe required in order for SNLS to detect these three events. We found the rate to be $\rho_{\rm slsn} = 91^{+76}_{-36}$ SNe yr^{-1} Gpc^{-3}. This measurement is consistent with what little was previously known about the rate of SLSNe, and, when combined with other measurements, the redshift evolution is consistent with that of the cosmic star-formation history. We estimated the rate of ULGRBs based on the published samples of these events and find their rate to be comparable with the rate of SLSNe at a similar redshifts further demonstrating that these events may be connected though a common progenitor. We have also studied the properties of the host galaxies associated with our SLSN candidates, and find them to be consistent with the distribution of the known sample of SLSNe.

ACKNOWLEDGMENTS

MS acknowledges support from EU/FP7-ERC grant no [615929].

This work is based on observations obtained with MegaPrime/MegaCam, a joint project of CFHT and CEA/DAPNIA, at the Canada-France-Hawaii Telescope (CFHT) which is operated by the National Research Council (NRC) of Canada, the Institut National des Sciences de l'Univers of the Centre National de la Recherche Scientifique (CNRS) of France, and the University of Hawaii. This work is based in part on data products produced at the Canadian Astronomy Data Centre as part of the Canada-France-Hawaii Telescope Legacy Survey, a collaborative project of NRC and CNRS.

Some of the data presented herein were obtained at the W.M. Keck Observatory, which is operated as a scientific partnership among the California Institute of Technology, the University of California and the National Aeronautics and Space Administration. The Observatory was made possible by the generous financial support of the W.M. Keck Foundation.

REFERENCES

Arcavi I., et al., 2016, ApJ, 819, 35
Arnett W. D., 1982, ApJ, 253, 785
Aspvall B., Stone R. E., 1980, Journal of Algorithms, 1, 1
Astier P., et al., 2006, A&A, 447, 31
Balland C., et al., 2009, A&A, 507, 85
Barbary K., et al., 2009, ApJ, 690, 1358
Bazin G., et al., 2009, A&A, 499, 653
Betoule M., et al., 2013, A&A, 552, A124
Blanton M. R., Roweis S., 2007, AJ, 133, 734
Bloom J. S., et al., 2011, Science, 333, 203
Boulade O., et al., 2003, in Iye M., Moorwood A. F. M., eds, Society of Photo-Optical Instrumentation Engineers (SPIE) Conference Series Vol. 4841, Instrument Design and Performance for Optical/Infrared Ground-based Telescopes. pp 72–81
Bronder T. J., et al., 2008, A&A, 477, 717
Brown G. C., Levan A. J., Stanway E. R., Tanvir N. R., Cenko S. B., Berger E., Chornock R., Cucchiaria A., 2015, MNRAS, 452, 4297
Burrows D. N., et al., 2011, Nature, 476, 421
Cenko S. B., et al., 2012, ApJ, 753, 77
Chatzopoulos E., Wheeler J. C., Vinko J., Horvath Z. L., Nagy A., 2013, ApJ, 773, 76
Chen T.-W., et al., 2013, ApJ, 763, L28
Chen T.-W., Smartt S. J., Yates R. M., Nicholl M., Krühler T., Schady P., Dennefeld M., Inserra C., 2016, preprint, (arXiv:1605.04925)
Chevalier R. A., Irwin C. M., 2011, ApJ, 729, L6
Chomiuk L., et al., 2011, ApJ, 743, 114
Cooke J., et al., 2012, Nature, 491, 228
Coward D. M., et al., 2012, MNRAS, 425, 2668
Drake A. J., et al., 2011, ApJ, 735, 106
Ellis R. S., et al., 2008, ApJ, 674, 51
Fakhouri H. K., 2013, PhD thesis, University of California, Berkeley
Feroz F., Hobson M. P., 2008, MNRAS, 384, 449
Feroz F., Hobson M. P., Bridges M., 2009, MNRAS, 398, 1601
Feroz F., Hobson M. P., Cameron E., Pettitt A. N., 2013, preprint, (arXiv:1306.2144)
Firth R. E., et al., 2015, MNRAS, 446, 3895
Gal-Yam A., 2012, Science, 337, 927
Garn T., Best P. N., 2010, MNRAS, 409, 421
Gehrels N., et al., 2004, ApJ, 611, 1005
Gendre B., et al., 2013, ApJ, 766, 30
Gordon K. D., Clayton G. C., Misselt K. A., Landolt A. U., Wolff M. J., 2003, ApJ, 594, 279
Greiner J., et al., 2015, Nature, 523, 189
Guy J., et al., 2010, A&A, 523, A7
Hopkins A. M., Beacom J. F., 2006, ApJ, 651, 142
Howell D. A., et al., 2005, ApJ, 634, 1190
Howell D. A., et al., 2013, ApJ, 779, 98
Howell E. J., Coward D. M., Stratta G., Gendre B., Zhou H., 2014, MNRAS, 444, 15
Ilbert O., et al., 2006, A&A, 457, 841
Inserra C., Smartt S. J., 2014, ApJ, 796, 87
Inserra C., et al., 2013, ApJ, 770, 128
Inserra C., et al., 2016, preprint, (arXiv:1604.01226)
Jakobsson P., et al., 2006, A&A, 447, 897
Jakobsson P., et al., 2012, ApJ, 752, 62
Kasen D., Bildsten L., 2010, ApJ, 717, 245
Khachiyan L., 1980, USSR Computational Mathematics and Mathematical Physics, 20, 53
Le Borgne D., Rocca-Volmerange B., 2002, A&A, 386, 446
Le Fèvre O., et al., 2013, A&A, 559, A14
Leloudas G., et al., 2015, MNRAS, 449, 917
Levan A. J., et al., 2011, Science, 333, 199
Levan A. J., Read A. M., Metzger B. D., Wheatley P. J., Tanvir N. R., 2013, ApJ, 771, 136
Levan A. J., et al., 2014, ApJ, 781, 13
Levan A. J., et al., 2016, ApJ, 819, 51
Lidman C., et al., 2013, PASA, 30, e001
Lilly S. J., et al., 2007, ApJS, 172, 70
Lunnan R., et al., 2013, ApJ, 771, 97
Lunnan R., et al., 2014, ApJ, 787, 138
Lunnan R., et al., 2015, ApJ, 804, 90
Mazzali P. A., McFadyen A. I., Woosley S. E., Pian E., Tanaka M., 2014, MNRAS, 443, 67
Mazzali P. A., Sullivan M., Pian E., Greiner J., Kann D. A., 2016, MNRAS, 458, 3455
McCrum M., et al., 2014, MNRAS, 437, 656
McCrum M., et al., 2015, MNRAS, 448, 1206
Neill J. D., et al., 2006, AJ, 132, 1126
Neill J. D., et al., 2011, ApJ, 727, 15
Nicholl M., Smartt S. J., 2015, preprint, (arXiv:1511.03740)

Nicholl M., et al., 2013, Nature, 502, 346
Nicholl M., et al., 2014, MNRAS, 444, 2096
Nicholl M., et al., 2015a, MNRAS, 452, 3869
Nicholl M., et al., 2015b, ApJ, 807, L18
Ofek E. O., et al., 2007, ApJ, 659, L13
Papadopoulos A., et al., 2015, MNRAS, 449, 1215
Pastorello A., et al., 2010, ApJ, 724, L16
Perrett K., et al., 2010, AJ, 140, 518
Perrett K., et al., 2012, AJ, 144, 59
Quimby R. M., Aldering G., Wheeler J. C., Höflich P., Akerlof C. W., Rykoff E. S., 2007, ApJ, 668, L99
Quimby R. M., et al., 2011, Nature, 474, 487
Quimby R. M., Yuan F., Akerlof C., Wheeler J. C., 2013, MNRAS, 431, 912
Smith N., et al., 2007, ApJ, 666, 1116
Smith M., et al., 2016, ApJ, 818, L8
Sorokina E., Blinnikov S., Nomoto K., Quimby R., Tolstov A., 2015, preprint, (arXiv:1510.00834)
Sullivan M., et al., 2006, AJ, 131, 960
Sullivan M., et al., 2011, ApJ, 737, 102
Thöne C. C., et al., 2011, Nature, 480, 72
Vreeswijk P. M., et al., 2014, ApJ, 797, 24
Walker E. S., et al., 2011, MNRAS, 410, 1262
Wang S. Q., Wang L. J., Dai Z. G., Wu X. F., 2015, ApJ, 799, 107
Woosley S. E., 2010, ApJ, 719, L204
Woosley S. E., Blinnikov S., Heger A., 2007, Nature, 450, 390
Yan L., et al., 2015, ApJ, 814, 108
York D. G., et al., 2000, AJ, 120, 1579
Zhang B.-B., Zhang B., Murase K., Connaughton V., Briggs M. S., 2014, ApJ, 787, 66

This paper has been typeset from a TEX/LATEX file prepared by the author.

APPENDIX A: SLSN PARAMETER SPACE

We choose an ellipsoid to define the parameter space of SLSNe in terms of the three main fit parameters of the magnetar model, $\tau_{\rm m}$, B_{14} and $P_{\rm ms}$. A position, in Cartesian coordinates, on a generic ellipsoid can be defined using equation A1.

$$\begin{pmatrix} x \\ y \\ z \end{pmatrix} = \mathbf{A} \begin{pmatrix} R_x \cos(u)\cos(v) \\ R_y \cos(u)\sin(v) \\ R_z \cos(v) \end{pmatrix} + \mathbf{C} \tag{A1}$$

where $\mathbf{A}$ is a rotation matrix, $\mathbf{R}$ is the radius of the ellipsoid and $\mathbf{C}$ is its center. The following conditions must be satisfied: $-\pi/2 \leq u \leq \pi/2$ and $-\pi \leq v \leq \pi$. We have set up our parameter space with $\tau_{\rm m}$ along the x-axis, B_{14} along the y-axis and $P_{\rm ms}$ corresponding to the z-axis. Using the Khachiyan Algorithm (Aspvall & Stone 1980; Khachiyan 1980), we have performed a fit to find an ellipsoid that best describes the known population of SLSNe. We found the ellipsoid to have the following properties:

$$\mathbf{A} = \begin{pmatrix} -0.184 & 0.575 & -0.797 \\ 0.008 & 0.812 & 0.586 \\ 0.983 & 0.102 & -0.154 \end{pmatrix} \tag{A2}$$

$$\mathbf{R} = \begin{pmatrix} R_x \\ R_y \\ R_z \end{pmatrix} = \begin{pmatrix} 1.89 \\ 2.17 \\ 11.32 \end{pmatrix} \tag{A3}$$

$$\mathbf{C} = \begin{pmatrix} 26.76 \\ 2.14 \\ 2.77 \end{pmatrix} \tag{A4}$$

APPENDIX B: LIGHT CURVES

Table B1. AB photometry of SNLS-07D3bs

MJD	Phase	g_M	r_M	i_M	z_M
54140.5	-42.4		23.59 (0.07)	23.33 (0.08)	23.63 (0.19)
54144.5	-38.4	23.42 (0.03)	23.22 (0.04)	23.04 (0.05)	
54151.5	-31.4	22.70 (0.02)	22.59 (0.03)	22.57 (0.04)	22.54 (0.11)
54153.5	-29.4	22.58 (0.02)	22.43 (0.02)	22.41 (0.03)	
54172.6	-10.3			21.62 (0.04)	
54176.4	-6.5	22.02 (0.01)	21.73 (0.01)	21.62 (0.02)	21.57 (0.04)
54179.5	-3.4	22.07 (0.01)	21.73 (0.01)	21.59 (0.02)	21.66 (0.03)
54183.5	0.6	22.17 (0.02)	21.75 (0.01)	21.60 (0.02)	
54186.4	3.5	22.22 (0.02)	21.76 (0.02)	21.56 (0.02)	21.49 (0.03)
54197.5	14.6		21.94 (0.03)	21.63 (0.02)	21.59 (0.05)
54201.4	18.5	22.70 (0.02)	21.99 (0.02)	21.68 (0.03)	
54205.4	22.5	22.82 (0.02)	22.05 (0.03)	21.70 (0.02)	21.62 (0.04)
54209.4	26.5	22.95 (0.02)	22.18 (0.02)	21.74 (0.02)	
54213.5	30.6	23.10 (0.06)	22.28 (0.02)	21.79 (0.02)	21.69 (0.05)
54229.4	46.5	23.86 (0.07)	22.71 (0.03)	22.12 (0.02)	21.85 (0.19)
54230.3	47.4				21.87 (0.07)
54233.3	50.4			22.11 (0.08)	
54234.4	51.5	24.05 (0.05)	22.92 (0.03)	22.26 (0.07)	
54251.4	68.5		23.63 (0.13)	22.68 (0.05)	22.16 (0.08)
54255.3	72.4	25.05 (0.34)	23.65 (0.08)	22.72 (0.09)	
54259.3	76.4	25.47 (0.14)	23.92 (0.11)	22.83 (0.03)	22.42 (0.08)
54262.4	79.5	25.60 (0.20)	23.90 (0.07)	22.91 (0.10)	
54266.3	83.4	25.68 (0.35)	24.20 (0.15)	23.01 (0.04)	22.40 (0.08)

This paper has been typeset from a TEX/LATEX file prepared by the author.